

**STUDIES ON THE PHOTOELECTROCHEMICAL
SPLITTING OF WATER FOR HYDROGEN GENERATION
WITH Cu_2O AND BiVO_4 BASED PHOTOELECTRODES**

IQRA REYAZ HAMDANI



**DEPARTMENT OF CHEMICAL ENGINEERING
INDIAN INSTITUTE OF TECHNOLOGY DELHI**

DECEMBER 2020

**STUDIES ON THE PHOTOELECTROCHEMICAL
SPLITTING OF WATER FOR HYDROGEN GENERATION
WITH Cu_2O AND BiVO_4 BASED PHOTOELECTRODES**

by

IQRA REYAZ HAMDANI

Department of Chemical Engineering

Submitted

in partial fulfilment of the requirements of the degree of Doctor of Philosophy
to the



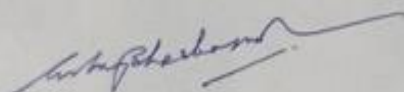
INDIAN INSTITUTE OF TECHNOLOGY DELHI

DECEMBER 2020

Dedicated to Faizan & my family ...

CERTIFICATE

This is to certify that the dissertation entitled "**Studies on the photoelectrochemical splitting of water for hydrogen generation with Cu_2O and BiVO_4 based photoelectrodes**" being submitted by **Ms. Iqra Reyaz Hamdani** to the Department of Chemical Engineering, Indian Institute of Technology Delhi, for fulfillment of the requirements for the award of **Doctor of Philosophy** in Chemical Engineering, is a record of bonafide research work carried out by her. She has worked under my supervision and has fulfilled the requirements, which to my knowledge, has reached the requisite standard for the submission of the thesis. The research reports and results presented in this thesis have not been submitted, in part or full, to any other university or institute for the award of any degree or diploma.



Ashok N. Bhaskarwar

Professor,
Department of Chemical Engineering,
Indian Institute of Technology Delhi
Hauz Khas, New Delhi - 110016
India

ACKNOWLEDGEMENTS

All praise is due to Almighty Allah (SWT) who is the Lord of the worlds, the most beneficent, the most merciful. As I am ending my journey of Ph.D. at IIT Delhi, it reminds me of my first day of work here as a research scholar. I bow down to Allah in gratitude for bestowing me with the opportunity, commitment, and energy to put in my best in fulfilling this aspiration that has evolved me in ways I never anticipated, and for blessing me with strength and positivity in the times of ups and downs of life. I am thankful to the Almighty for blessing me with the most caring and supportive family who always stands like a pillar in times of need and endorse every decision that I make.

I would like to express my sincere and heartfelt gratitude to my advisor Professor Ashok N. Bhaskarwar for his continuous support, encouragement, motivation, and above all his belief in me that I was capable of meeting his expectations. He was always there to motivate me and inspire me with his passion for research. His continuous guidance, contributions of time, and ideas are the root-cause of making my Ph.D. journey productive and stimulating. There have been several tough times in the pursuit of Ph.D., but he always showed his confidence in me. His hardworking and ardent inclination towards research would always leave an influential mark on my mind. He always tried his best to clear my doubts and evaluate my work whenever I needed it. I thank him for being a good critique and an admirer at the same time. This has transformed me in a manner I had never imagined. This research would not have been possible without his continuous support, and encouragement.

This journey of Ph.D. has been an evolutionary and a life-changing experience which would not have been possible without the contributions and guidance that I received from many people.

Besides my supervisor, I would like to thank my student research committee members (Prof.

Anupam Shukla, Prof. Ratan Mohan, and Prof. Kedar Khare) for their scholarly inputs, valuable advice, and mostly for the grilling questioning and criticism that motivated me to broaden my research from various perspectives.

I acknowledge my debt and gratitude to Prof. Emeritus Ashok Kumar Gupta for his academic guidance and for providing the necessary inputs towards writing and improving this thesis. My sincere thanks to him for sharing his knowledge and giving the valuable suggestions. I am highly thankful to Prof. R.D. Tarey for always making himself available despite his busy schedule, for listening to my queries and providing solutions and guiding me through the fundamentals and know-how of the technical problems associated with this thesis.

I would like to express my deep gratitude to Dr. Garima Dwivedi for helping me with the understanding of the fundamentals and the experimental know-how.

I am thankful to my friends Dr. Iyman Abrar and Dr. Arunima Shukla for their continuous emotional and professional support during all the times of highs and lows of my Ph.D. journey. I feel blessed for friends like them for their immense love, care, and understanding apart from the encouraging and exciting discussions.

I extend my sincere thanks to all my lab mates and seniors, Dr. Divya, Dr. Parsanta, Dr. Guncha, Dr. Sangeeta, Dr. Neha, Dr. Manisha, Mr. H.C. Dutta, Ms. Sony, Ms. Nituparna, Ms. Isha, and Mr. Priyank for their constant moral support and for making lab environment cordial.

I would also like to extend my thanks to Ms. Manju and Mr. Sanjay for their support and assistance in the lab during the course of my Ph.D.

I acknowledge my sincere gratitude to Ms. Nusrat Rashid, who has a special place in my heart and a very special contribution to my Ph.D. Whether it was helping me in tough times or motivating me through rough phases of this journey, she has always stood up as a sincere friend. Besides her, I want to express my sincere gratitude to Dr. Bajjnath, Dr. Pankaj Tiwari, and Dr. Kaisar for stimulating discussions and time to time scientific guidance.

I thank my sisters - Ms. Ayesha, Ms. Sufia, Dr. Uzma, Dr. Ieba, Ms. Firdous, Dr. Fatima, and Dr. Sanya for being so loving and caring. I wish them all happiness, health and success.

I gratefully acknowledge IIT Delhi for financial support through the IIT Delhi fellowship that made this Ph.D. journey possible. I extend my gratitude to the Head of Department, Chemical Engineering, and all the faculty Indian Institute of Technology Delhi for their contributions through direct and indirect support. My sincere thanks to the entire administrative and technical staff members of IIT Delhi who have been kind enough to contribute in their respective roles.

The journey of a Ph.D. is always a long one where it is easy to feel unmotivated for certain stretches of time. When the going gets tough, the best remedy is to have a family who extends their unending support to keep you motivated. I am indebted to my family for their love, care, understanding, and support throughout my life. This research would not have been possible without their blessings and prayers. I am thankful to my parents (Mrs. Basharat Jabeen and Mr. Reyaz Ahmad Hamdani) for all their sacrifices and support in fulfilling my dreams and longing to see this achievement come true. I pray for their health and happiness. I would like to express my deepest appreciation to my brother Mr. Masroor for having faith in me in every possible way and Mr. Wasif for sharing laughter, joy, and time together.

Faizan... thank you very much for being by my side in all good and bad times. Your prayers, best wishes and never ending support has made my life shine and my heart smile. Thank you for your trust, encouragement and your confidence in me. You have a huge contribution in motivating me both professionally and personally. This life has got a beautiful meaning because of your presence in it.

Iqra Reyaz Hamdani

December 2020

ABSTRACT

Solar energy is the largest reservoir of energy that can be utilized to address the current energy crisis and rising energy demands. One of the most attractive ways to harness solar energy is to directly convert it into a storable, renewable, and sustainable fuel, such as hydrogen. One promising approach is to use a photoelectrochemical (PEC) monolithic device where the light-absorption and electrolysis of water both occur at the same place.

In this thesis, modified Cu_2O (Cu_2O nanowires based p-n homojunction/ $\text{KTaO}_3/\text{MoS}_2$) and BiVO_4 (Mo-W doped $\text{BiVO}_4/\text{Co-Pi}/\text{NiFeO}_x$) based photoelectrodes are being suggested as the promising photoelectrode materials for the photoelectrochemical water-splitting for H_2 production. Detailed investigations were carried out on both Cu_2O and BiVO_4 to determine the factors responsible for limiting their water-splitting capabilities. Certain plausible solutions were suggested and efforts were made to address the critical issues, such as overpotential losses due to the rapid recombination of photogenerated charge carriers. Various modifications to the Cu_2O photocathode were carried out, such as the formation of 1-D Cu_2O structures in the form of nanowires, development of a buried Cu_2O p-n homojunction, overlayering with KTaO_3 , and co-catalyzing with MoS_2 . Improvements to BiVO_4 were also done to enhance its photocatalytic performances, such as doping with Mo and W, improving OER kinetics by co-catalyzing with Co-Pi and NiFeO_x . A conventional dye-sensitized solar cell (DSSC) was developed based on the TiO_2 working electrode and Pt counter electrode.

The planar unmodified Cu_2O photocathode was capable of generating only -2.82 mA/cm^2 of photocurrent density at 0 V vs. RHE, resulting in only 62% of Faradaic efficiency. The performance was enhanced when the size-scale was changed to 1-D where the current density obtained the value of -3.97 mA/cm^2 at 0 V vs. RHE, and raising the Faradaic efficiency to 82%. Formation of Cu_2O nanowires based p-n homojunction resulted in the generation of photovoltage of +0.9 V vs. RHE, and improved the photocurrent density to -7.42 mA/cm^2 at 0

V vs. RHE. A surface protective layer of KTaO_3 was applied on to the best performing photocathode sample, and a layer of 199 nm of KTaO_3 improved the photostability of Cu_2O to 84 hours under illumination. Co-catalyzing the protected Cu_2O with MoS_2 caused the photocurrent density to increase drastically to -11.1 mA/cm^2 at 0 V vs. RHE in an electrolyte of pH 4, in the presence of ethanol as a sacrificial agent. The Faradaic efficiency of the modified Cu_2O was 95%, producing around 186 mmol/cm^2 of H_2 for 84 hours under illumination.

Photocatalytic properties of BiVO_4 were observed to increase by doping with Mo and co-doping with W in the weight ratio of 1:1, where the photocurrent density achieved was 4.27 mA/cm^2 at 1.23 V vs. RHE. Co-catalyzing the doped BiVO_4 with Co-Pi raised the value of current density to 5.6 mA/cm^2 at 1.23 V vs. RHE while maintaining the stability for 12 hours under illumination. Coating of the modified BiVO_4 with an excellent OER photocatalyst NiFeO_x was observed to increase the current density to 6.21 mA/cm^2 at 1.23 V vs. RHE. The developed photoanode was stable for 32 hours in an electrolyte of pH of 9 and 18 hours at a pH of 4. The applied bias-to-photon efficiency (ABPE) of the developed photoanode was 2.48% which is the highest ABPE achieved for BiVO_4 . The in-house built DSSC exhibited the conversion efficiency of 6.7% with 0.8 V as the open-circuit voltage.

A stand-alone PEC device employing the developed Cu_2O photocathode and BiVO_4 photoanode, and driven by an in-house built dye-sensitized solar cell (DSSC) was fabricated and tested towards the hydrogen generation. The current density produced by the constructed PEC device was around -5.8 mA/cm^2 at 0 V vs. RHE in the pH of 4 with the stability for 15.2 hours under illumination. The un-assisted solar-to-hydrogen (STH) conversion efficiency of 3.3% was achieved, thereby setting a benchmark for a PEC device based on Cu_2O and BiVO_4 photoelectrodes.

सार

सौर ऊर्जा ऊर्जा का सबसे बड़ा भंडार है जिसका उपयोग वर्तमान ऊर्जा संकट और बढ़ती ऊर्जा मांगों को संबोधित करने के लिए किया जा सकता है। सौर ऊर्जा का दोहन करने के सबसे आकर्षक तरीकों में से एक इसे सीधे तौर पर एक हवादार, नवीकरणीय और टिकाऊ ईंधन में बदलना है, जैसे हाइड्रोजन। एक आशाजनक दृष्टिकोण एक फोटोइलेक्ट्रॉनिक (PEC) अखंड डिवाइस का उपयोग करना है जहां प्रकाश-अवशोषण और पानी के इलेक्ट्रोलिसिस दोनों एक ही स्थान पर होते हैं।

इस थीसिस में, संशोधित Cu_2O (Cu_2O nanowires pn homojunction पर KTaO_3 / MoS_2) और BiVO_4 (Mo-W doped BiVO_4 / Co-Pi / NiFeOx) पर आधारित फोटोइलेक्ट्रोड को फोटोइलेक्ट्रॉनिक वाटर-स्प्लिटिंग के लिए आशाजनक फोटोइलेक्ट्रोड सामग्री के रूप में सुझाया जा रहा है। उनकी पानी-बंटवारे की क्षमताओं को सीमित करने के लिए जिम्मेदार कारकों का निर्धारण करने के लिए Cu_2O और BiVO_4 दोनों पर विस्तृत जांच की गई। कुछ प्रशंसनीय समाधान सुझाए गए थे और महत्वपूर्ण मुद्दों को संबोधित करने के प्रयास किए गए थे, जैसे कि फोटोजेनरेटेड चार्ज वाहकों के तेजी से पुनर्संयोजन के कारण अत्यधिक नुकसान। Cu_2O फोटोकैथोड के लिए कई संशोधन किए गए, जैसे कि nanowires के रूप में 1-D Cu_2O संरचनाओं का निर्माण, एक बरीड Cu_2O p-n होमोजिशन का विकास, KTaO_3 के साथ ओवरलेयरिंग, और MoS_2 के साथ सह-उत्प्रेरित होना। BiVO_4 में सुधार इसके फोटोकैटलिटिक प्रदर्शन को बढ़ाने के लिए भी किया गया था, जैसे कि Mo और W के साथ डोपिंग, Co-Pi और NiFeOx के साथ सह-उत्प्रेरक द्वारा OER कैनेटीक्स में सुधार करना। एक पारंपरिक डार्क-सेंसिटाइज्ड सोलर सेल (DSSC) को TiO_2 वर्किंग इलेक्ट्रोड और Pt काउंटर इलेक्ट्रोड के आधार पर विकसित किया गया था।

प्लेनर अनमोडिफाइड Cu_2O फोटोकैथोड 0 V vs RHE में केवल $-2.12 \text{ mA} / \text{cm}^2$ photocurrent घनत्व उत्पन्न करने में सक्षम था, जिसके परिणामस्वरूप केवल 62% फैराडिक दक्षता थी। प्रदर्शन को बढ़ाया गया था जब आकार-स्केल को 1-डी में बदल दिया गया था, जहां वर्तमान घनत्व ने 0 V बनाम आरएचएच पर $-3.96 \text{ mA} / \text{cm}^2$ का मूल्य प्राप्त किया था, और फैराडिक दक्षता को 82% तक बढ़ा दिया था। Cu_2O nanowires आधारित पी-एन होमोजिशन के गठन के परिणामस्वरूप, फोटोकॉल वोल्टेज +0.9 V बनाम RHE की उत्पत्ति हुई, और फोटोकल घनत्व में $-6.82 \text{ mA} / \text{cm}^2$ में 0 V

बनाम RHE में सुधार हुआ। KTaO_3 की एक सतह सुरक्षात्मक परत को सबसे अच्छा प्रदर्शन करने वाले फोटोकैथोड नमूने पर लागू किया गया था, और KTaO_3 के 199 nm की परत ने रोशनी के तहत Cu_2O की फोटोस्टेबिलिटी को 48 घंटे तक सुधार दिया। MoS_2 के साथ संरक्षित Cu_2O को सह-उत्प्रेरित करने से photocurrent घनत्व में पीएच 8 के एक इलेक्ट्रोलाइट में 0 V बनाम RHE पर एक एजेंट के रूप में इथेनॉल की उपस्थिति में $-11.1 \text{ mA} / \text{cm}^2$ में अत्यधिक वृद्धि हुई। संशोधित Cu_2O की फैराडिक दक्षता 99% थी, जो रोशनी के तहत 84 घंटों के लिए H_2 के 166 mmol / cm^2 का उत्पादन करती है।

BiVO_4 के Photocatalytic गुणों को 1: 1 के वजन अनुपात में Mo के साथ डोपिंग और W के साथ सह-डोपिंग द्वारा देखा गया , जहां प्राप्त फोटोकॉरेंट घनत्व 1.23 V बनाम RHE पर, 8.26 mA / cm^2 था । Co- Pi के साथ डोप किए गए BiVO_4 को सह-उत्प्रेरित करते हुए रोशनी के तहत 12 घंटे तक स्थिरता बनाए रखते हुए वर्तमान घनत्व का मान 1.23 V बनाम RHE पर 9.6 mA / cm^2 कर दिया गया। एक उत्कृष्ट OER फोटोकैटलिस्ट NiFeOx के साथ संशोधित BiVO_4 की कोटिंग के वर्तमान घनत्व को बढ़ाकर 1.23 V बनाम RHE पर 6.21 mA / cm^2 किया गया। विकसित फोटोएनोड 9 के पीएच और 8 पीएच पर इलेक्ट्रोलाइट में 32 घंटे के लिए स्थिर था। विकसित फोटोएनोड की लागू पूर्वाग्रह-से-फोटॉन दक्षता (ABPE) 2.8 is% थी जो BiVO_4 के लिए प्राप्त उच्चतम ABPE है । इन-हाउस में निर्मित DSSC ने ओपन-वोल्टेज वोल्टेज के रूप में 0.8 V के साथ 6.6% की रूपांतरण दक्षता का प्रदर्शन किया।

एक एकल-अकेले PEC यंत्र ने विकसित Cu_2O फोटोकैथोड और BiVO_4 फोटोएनोड को नियोजित किया है, और एक इन-हाउस निर्मित डार्क-सेंसिटाइज़्ड सोलर सेल (DSSC) द्वारा संचालित किया गया है और इसे हाइड्रोजन जेनरेशन की ओर टेस्ट किया गया है। निर्मित PEC यंत्र द्वारा निर्मित वर्तमान घनत्व रोशनी के तहत 15.2 घंटे की स्थिरता के साथ 8 के पीएच में 0 V बनाम RHE पर $-9.6 \text{ mA} / \text{cm}^2$ था। 3.3% की गैर असिस्टेड सोलर-टू-हाइड्रोजन (STH) रूपांतरण दक्षता हासिल की गई, जिससे Cu_2O और BiVO_4 फोटोइलेक्ट्रोड पर आधारित PEC यंत्र के लिए एक तल चिह्न स्थापित किया गया।

TABLE OF CONTENTS

CERTIFICATE	i
ACKNOWLEDGEMENTS	ii
ABSTRACT	v
TABLE OF CONTENTS	vii
LIST OF FIGURES	xii
LIST OF TABLES	xxi
LIST OF ABBREVIATIONS	xxiii
LIST OF ACRONYMS	xxiv
INTRODUCTION	1
1.1. ENERGY STORING TECHNOLOGIES	3
1.2. CONCEPTUAL CONFIGURATION OF A PEC DEVICE	5
1.2.1. Photocatalyst materials for PEC water splitting	7
1.2.2. Cuprous oxide (Cu ₂ O).....	8
1.2.3. Bismuth vanadate (BiVO ₄)	9
1.3. PROBLEM IDENTIFICATION	10
1.3.1. Learning from the literature	11
1.4. AIM AND SCOPE OF WORK.....	11
1.4.1. Objectives	12
1.5. STRUCTURE OF THE THESIS	13
LITERATURE REVIEW.....	15
2.1. INTRODUCTION.....	16
2.2. WORKING PRINCIPLE OF PHOTOELECTROCHEMICAL (PEC) WATER-SPLITTING	17
2.3. PHOTOELECTROCHEMICAL (PEC) PERFORMANCE EVALUATION PARAMETERS	19
2.3.1. Overall solar-to-hydrogen conversion efficiency (η_{STH}).....	19
2.3.2. Photocurrent density	21
2.3.3. Incident photon-to-current conversion efficiency (IPCE), or External Quantum Efficiency (EQE)	23

2.3.4.	Applied bias photon to current efficiency (ABPE), or Internal Quantum Efficiency	(IQE)	24
2.3.5.	System impedance		25
2.4.	BAND ENERGETICS AND BAND-EDGE POTENTIAL CONSIDERATIONS		26
2.5.	PHOTOELECTROCHEMICAL SEMICONDUCTOR MATERIALS		30
2.6.	PHOTOELECTROCHEMICAL REACTOR DESIGNS AND CONFIGURATIONS		38
2.6.1.	Single-photoelectrode PEC reactor		38
2.6.2.	Photo-reactors based on p-n junction electrodes		39
2.6.3.	Photo-reactors based on semiconductor/carbon photoelectrodes		41
2.6.4.	Photo-reactors based on dye-sensitized semiconductor electrodes (DS – PEC)		42
2.6.5.	PEC reactors based on dual-photoelectrodes tandem configuration		44
2.6.6.	Photoelectrochemical /photovoltaic tandem reactors		49
2.6.6.1.	PEC/conventional solar-cell system		49
2.6.6.2.	Multi-junction PEC/PV reactors		51
2.6.6.3.	PEC/DSSC reactor (this work)		52
2.7.	THEORETICAL STUDIES AND MODELS FOR EFFICIENT PEC WATER-SPLITTING		54
2.8.	CHALLENGES AND POSSIBLE SOLUTIONS		56
2.8.1.	Low unassisted STH conversion efficiency		56
2.8.2.	Photocorrosion due to self-oxidation/reduction		58
2.8.3.	PEC device design for optimum efficiency and cost		59
2.8.4.	Scale-up for the best practically-viable PEC devices		60
2.9.	CONCLUSIONS AND FUTURE PERSPECTIVE		62
	EXPERIMENTAL WORK		64
3.1.	DEVELOPMENT OF Cu ₂ O PHOTOCATHODE AND CORRESPONDING STUDIES ON THE PHOTOELECTROCHEMICAL SPLITTING OF WATER		66
3.1.1.	Materials and synthesis of intrinsic planar Cu ₂ O thin films		66
3.1.2.	Materials and synthesis of p-Cu ₂ O nanowires		72
3.1.3.	Materials and synthesis of Cu ₂ O nanowires based p-n homojunction		78
3.1.4.	Materials and synthesis of the protective overlayer of potassium tantalate (KTaO ₃)		81

3.1.5.	Materials and synthesis of HER co-catalyst - MoS ₂	83
3.2.	DEVELOPMENT OF BiVO ₄ PHOTOANODE AND CORRESPONDING STUDIES ON THE PHOTOELECTROCHEMICAL SPLITTING OF WATER.....	86
3.2.1.	Materials and syntheses of intrinsic BiVO ₄ (Monoclinic scheelite phase).....	87
3.2.1.1.	Solid-state reaction method	87
3.2.1.2.	Co-precipitation method	88
3.2.1.3.	Hydrothermal method.....	89
3.2.2.	Materials and syntheses of doped BiVO ₄ synthesized by solid-state method ..	91
3.2.3.	Materials and synthesis of Co-Pi co-catalyst for Mo-W doped BiVO ₄	92
3.2.4.	Photo-electrodeposition of an overlayer of NiFeO _x OEC for stability improvement.....	92
3.3.	PERFORMANCE EVALUATION AND TESTING.....	93
3.4.	SYNTHESIS AND FABRICATION OF A DYE-SENSITIZED SOLAR CELL (DSSC)	97
3.4.1.	Working electrode.....	98
3.4.2.	Counter electrode	99
3.4.3.	Electrolyte	99
3.4.4.	Fabrication of DSSC cell	99
3.4.5.	Photovoltaic performance evaluation and testing.....	100
3.5.	COUPLING OF THE DEVELOPED DSSC WITH THE PEC DEVICE EMPLOYING THE PREPARED Cu ₂ O BASED PHOTOCATHODE AND BiVO ₄ BASED PHOTOANODE	100
	RESULTS AND DISCUSSION	102
4.1.	PERFORMANCE EVALUATION AND DETAILED STUDIES ON Cu ₂ O PHOTOCATHODE TOWARDS THE HYDROGEN PRODUCTION VIA PHOTOELECTROCHEMICAL WATER SPLITTING.....	103
4.1.1.	Planar intrinsic Cu ₂ O	103
4.1.1.1.	Effect of bath pH on the structural, morphological, optoelectronic, and photoelectrochemical properties of electrodeposited Cu ₂ O.....	103
4.1.1.2.	Effect of deposition potential on the structural, morphological, optoelectronic and photoelectrochemical properties of electrodeposited Cu ₂ O.....	127
4.1.1.3.	Effect of deposition time on the structural, morphological, optoelectronic and photoelectrochemical properties of electrodeposited Cu ₂ O.....	136
4.1.2.	p-Cu ₂ O nanowires.....	149

4.1.2.1.	Effect of the magnetic field strength on the nanowires' alignment and size-distribution	149
4.1.2.2.	Effect of annealing temperature on the photocatalytic properties of p-Cu ₂ O nanowires.....	155
4.1.3.	Cu ₂ O nanowires based p-n homojunction.....	159
4.1.4.	KTaO ₃ protected Cu ₂ O nanowires based p-n homojunction and co-catalyzed with MoS ₂ (p-Cu ₂ O/n-Cu ₂ O /KTaO ₃ /MoS ₂)	168
4.1.5.	Physical characterizations and performance evaluations of the modified cathode	179
4.1.6.	Corrosion studies	184
4.1.6.1.	Analysis of the crystallographic composition before and after HER reaction	185
4.1.6.2.	Analysis of the surface morphology before and after HER reaction.....	185
4.1.6.3.	Analysis of surface morphology before and after the HER reaction using an optical microscope	186
4.2.	PERFORMANCE EVALUATION AND DETAILED STUDIES ON BiVO ₄ PHOTOANODE TOWARDS THE OXYGEN EVOLUTION REACTION VIA PHOTOELECTROCHEMICAL WATER SPLITTING.....	187
4.2.1.	Intrinsic BiVO ₄ (monoclinic scheelite phase).....	188
4.2.1.1.	BiVO ₄ synthesized from solid-state reaction method.....	188
4.2.1.2.	BiVO ₄ synthesized from co-precipitation method.....	190
4.2.1.3.	BiVO ₄ synthesized from the hydrothermal method	191
4.2.2.	BiVO ₄ synthesized by the solid-state method and doped with Mo, W, and co-doped with Mo-W.....	193
4.2.3.	Mo-W doped BiVO ₄ /Co-Pi.....	195
4.2.4.	Mo:W doped BiVO ₄ /Co-Pi/ NiFeO _x	200
4.2.5.	Comparative analyses of pristine BiVO ₄ and the modified BiVO ₄	204
4.3.	DYE-SENSITIZED SOLAR CELL (DSSC).....	214
4.4.	PERFORMANCE EVALUATION OF THE COUPLED SYSTEM OF DEVELOPED PEC DEVICE EMPLOYING THE PREPARED Cu ₂ O BASED PHOTOCATHODE AND BIVO ₄ BASED PHOTOANODE WITH THE IN-HOUSE BUILT DSSC.....	218
4.4.1.	Photovoltaic measurements of the two DSSCs combined in series.....	218
4.4.2.	Photoelectrochemical performance of the PEC device coupled to the two DSSCs in a series configuration.....	220

4.4.3. Stability analysis and H ₂ generation	221
CONCLUSIONS AND RECOMMENDATIONS FOR FURTHER WORK.....	225
5.1. SUMMARY AND CONCLUSIONS	226
5.1.1. Summary	226
5.1.2. Conclusions.....	228
5.2. OUTCOME OF THE RESEARCH WORK.....	231
5.3. RECOMMENDATIONS FOR FURTHER WORK.....	232
REFERENCES.....	233
APPENDICES	266

LIST OF FIGURES

Figure 1.1. An outlook of the worldwide energy consumption and the projected energy consumption up to the year 2050. (“U.S.. Energy Information Administration (EIA)- International energy outlook 2019,” 2019).....	2
Figure 1.2. Current commercial hydrogen production technologies (“U.S. Drive in partnership with U.S. Department of Energy (DOE),” 2020).	5
Figure 1.3. A basic model of a PEC reactor with anode as the photoactive semiconductor carrying out the OER and cathode performing the HER. V is the external bias, d is the width of the depletion region, $h\nu$ is the incident solar light, E_g is the bandgap of the anode, h^+ is the photogenerated holes, and e^- is the photogenerated electrons.	6
Figure 1.4. Schematic representation of energy band-edges of Cu_2O	9
Figure 1.5. Schematic representation of energy band-edges of $BiVO_4$	10
Figure 1.6. Key features of the PEC device.	12
Figure 2.1. Working principle of a photoelectrochemical device.	17
Figure 2.2. Effect of the external biasing on the band-edge positions of a photo-anode. (i) electrode at flatband potential, (ii) electrode at the potential $<$ flatband potential, (iii) electrode at potential $>$ flatband potential, (iv) electrode at a large reverse-bias potential, causing the saturation of photocurrent. In regions (iii) and (iv), the downward band bending for an n-type semiconductor can be seen under anodic-bias conditions. The corresponding j-v plot is given to the right of the figure (chen et al., 2013a).	23
Figure 2.3. A typical nyquist plot used for the electrochemical impedance measurements. ...	26
Figure 2.4. Influence of the bandgap on inherent theoretical STH efficiencies of photoelectrodes.	27
Figure 2.5. Bandgap values and band-edge positions of some of the widely studied photoelectrodes.	28
Figure 2.6. Recommended flowchart for a single photo-electrode based PEC device (Chen et al., 2010).	30
Figure 2.7. PEC device with one photo-absorbing semiconductor electrode (photoanode) (Yang et al., 2017).	38
Figure 2.8. Performance of a PEC device based on $MoS_2 - rGO$ photoelectrode (Barman et al., 2017).	41

Figure 2.9. Illustration of the working principle of a photo-reactor based on dye-sensitized semiconductor electrode (DS-PEC) (Z. Yu et al., 2015a).	44
Figure 2.10. PEC reactors based on the dual-photoelectrodes system, (a) parallel arrangement of photoelectrodes, (b) back-to-back arrangement of photoelectrodes (Peerakiathajohn et al., 2016).	46
Figure 2.11. Conceptual diagram of a pec/pv tandem reactor in (a) dual-photoelectrode system, (b) single-photoelectrode system (Miller et al., 2003).	50
Figure 2.12. Conceptual diagram of a PEC/DSSC tandem reactor (Gan et al., 2014).	53
Figure 2.13. Reduction of bandgap by N substitution in a photoactive semiconductor material (Meng et al., 2012)	58
Figure 2.14. Schematic diagram of a lab-scale reactor system based on photocatalyst coated quartz tubes filled with optical fibers (Ray et al., 1998).	61
Figure 2.15. Schematic diagram of the repeating base-units of solar water-splitting modules developed by Turan and co-workers. This figure is adapted from reference (Turan et al., 2016).	62
Figure 3.1. The organization of experimental work.	65
Figure 3.2. Schematic representation of the cleaning procedure of the FTO substrates.	68
Figure 3.3. Schematic diagram of the synthesis procedure of Cu ₂ O thin films via electrodeposition method.	69
Figure 3.4. Digital images of FTO substrate (a) and thin film of Cu ₂ O electrodeposited on FTO substrate (b)	69
Figure 3.5. Schematic diagram showing the cleaning process of Cu substrates.	73
Figure 3.6. Cyclic voltammetry plots to determine the anodization potential for Cu in a 3 M KOH solution.	74
Figure 3.7. Digital photographs of Cu(OH) ₂ nanowires (a), and Cu ₂ O nanowires (b).	75
Figure 3.8. Schematic diagram representing the synthesis of p-Cu ₂ O nanowires.	76
Figure 3.9. Schematic diagram showing the protective effect of a thin film of planar p-Cu ₂ O over the nanowires (Luo et al., 2016b).	77
Figure 3.10. Schematic diagram showing the fabrication of Cu ₂ O nanowires based p-n homojunction (a), and current vs. time response of photo-electrodeposition of n-Cu ₂ O over the surface of p-Cu ₂ O nanowires (b).	80
Figure 3.11. Schematic representation of the synthesis of KTaO ₃ powder by hydrothermal method.	82

Figure 3.12. Digital image of the synthesized KTaO_3 powder.	82
Figure 3.13. Schematic representation of photo-electrodeposition of MoS_2 on Cu/ Cu_2O p-n homojunction/ KTaO_3	85
Figure 3.14. Photographic images of photo-electrodeposited MoS_2 on Cu/ Cu_2O p-n homojunction/ KTaO_3 (a) without N_2 purging, (b) with N_2 purging.....	86
Figure 3.15. Schematic diagram representing the synthesis of BiVO_4 by solid-state reaction method.	87
Figure 3.16. Digital image of the prepared pure BiVO_4 synthesized by solid-state reaction method.	88
Figure 3.17. Schematic diagram representing the synthesis of BiVO_4 by solid-state reaction method.	88
Figure 3.18. Digital images of the synthesis procedure of pure BiVO_4 by co-precipitation method.	89
Figure 3.19. Schematic diagram representing the synthesis of BiVO_4 by hydrothermal method.	89
Figure 3.20. Digital image of the prepared yellow solution from solution a and solution b mixture.....	90
Figure 3.21. Digital image of the drop-casted BiVO_4 thin film onto the FTO substrate.....	90
Figure 3.22. Digital image of the collection of H_2 gas in a two-electrode set-up.....	96
Figure 3.23. Experimental set-up for the characterization and performance evaluations of the working electrodes (a), and set-up for the H_2 gas collection in a two-electrode electrochemical cell (b).	97
Figure 3.24. Schematic diagram of the deposition of Pt film onto the FTO (a), and the digital image of the calcined Pt film onto the FTO substrate at 450°C (b).	99
Figure 3.25. Schematic diagram of the assembled DSSC (a), and a digital image of the assembled DSSC (b).....	1000
Figure 3.26. Experimental set-up for the coupled PEC device and the in-house built DSSC.	101
Figure 4.1. Current density vs. time response of electrodeposition of Cu_2O in 0.05 M at various electrolyte pH values.	104
Figure 4.2. Influence of the deposition pH on the electrodeposited film thickness of Cu_2O .	105
Figure 4.3. XRD peaks analysis of Cu_2O electrodeposited at various bath pH values.....	106

Figure 4.4. Enlarged (111) diffraction profiles for Cu ₂ O films synthesized at various bath pH.	107
Figure 4.5. Determination of FWHM of (111) peaks of Cu ₂ O using the Gaussian function.	108
Figure 4.6. SEM micrographic images of electrodeposited thin films of Cu ₂ O at bath pH values of (a) 5, (b) 6, (c) 7, (d) 8, (e) 9, and (f) 10.	110
Figure 4.7. W-H plot for Cu ₂ O films electrodeposited at various bath pH.	112
Figure 4.8. Cumulative Gaussian fit to diffraction peaks for determination of W-H plots of Cu ₂ O films electrodeposited at various bath pH.	113
Figure 4.9. Determination of UV-visible absorbance spectra (a), and estimation of bandgaps from the Tauc plots (b), of Cu ₂ O films deposited at various electrolyte pH values.....	114
Figure 4.10. Mott-schottky plots of Cu ₂ O films deposited at various electrolyte pH values in 0.5 M Na ₂ SO ₄ electrolyte under dark conditions.	118
Figure 4.11. Influence of the deposition pH on the positions of the band-edges of Cu ₂ O. ...	122
Figure 4.12. Photoelectrochemical measurement of Cu ₂ O in 0.5 M Na ₂ SO ₄ in terms of photocurrent density generation, electrodeposited at the bath pH from 5 to 10.....	124
Figure 4.13. (a) Estimation of charge transfer resistance of electrodeposited Cu ₂ O films at various electrolyte pH values. Inset is the equivalent fitting circuit corresponding to the Nyquist plots (b) Impedance values at higher frequencies.	125
Figure 4.14. Determination of reduction potential window of 0.05 M CuSO ₄ .5H ₂ O + 3 M lactic acid (pH 9) by the cyclic voltammetry analysis.	127
Figure 4.15. Current vs. time response for the electrodeposition of Cu ₂ O at various deposition potentials.....	128
Figure 4.16. XRD peaks for electrodeposited Cu ₂ O at various deposition potentials.	130
Figure 4.17. SEM micrographs of Cu ₂ O films deposited at (a) -0.2 V, (b) -0.3 V, (c) -0.4 V, (d) -0.5 V, and (e) -0.6 V.....	131
Figure 4.18. (a) Absorption spectra of Cu ₂ O thin films using UV-visible spectrophotometer, (b) determination of bandgap by Tauc plot.	133
Figure 4.19. Determination of the type of conductivity and charge carrier densities of Cu ₂ O samples deposited at various deposition potentials via Mott-Schottky plots.....	134
Figure 4.20. Photoelectrochemical performances in terms of photocurrent density generation, (a) and analysis of impedance spectroscopy through Nyquist plots (b), of Cu ₂ O thin films deposited at different potentials in 0.5 M Na ₂ SO ₄ (pH 8).....	136
Figure 4.21. Current vs. time response of electrodeposition of Cu ₂ O thin films for various deposition time periods.....	137

Figure 4.22. XRD analysis of Cu ₂ O thin films deposited for various time periods.	139
Figure 4.23. W-H plots for lattice strain determination.	140
Figure 4.24. SEM micrographic images of Cu ₂ O samples deposited for (a) 15 min, (b) 20 min, (c) 25 min, (d) 30 min, (e) 35 min, and (f) 40 min.	142
Figure 4.25. Analysis of the light absorption spectra by UV-visible spectroscopy (a), and determination of bandgaps by the Tauc plot (b).	142
Figure 4.26. Electrochemical impedance analysis by Nyquist plots, in 0.5 M Na ₂ SO ₄	144
Figure 4.27. Determination of the type of conductivity, flatband potentials, and charge carrier densities with respect to the deposition times.	145
Figure 4.28. Photocurrent density determination by Cu ₂ O thin films electrodeposited at various time periods.	146
Figure 4.29. Stability analysis of the best performing Cu ₂ O sample in an electrolyte of pH 6 under illumination (a), and amount of H ₂ generation determination by the GC analysis.	148
Figure 4.30. The overall size distribution of p-Cu ₂ O nanowires grouped in 1 μm length ranges from 1 to 5 μm (a), FESEM images of p-Cu ₂ O nanowires samples synthesized at various magnetic field strengths (b-e) observed at a magnification of 100 kX.	151
Figure 4.31. TEM micrographs of p-Cu ₂ O nanowires synthesized under different magnetic fields. The red lines indicate the direction of the magnetic fields.	152
Figure 4.32. Angular distribution diagrams for the normalized number of nanowires corresponding to the nanowire-length group of 0 – 1 μm, 1-2 μm, 2-3 μm, 3-4 μm, and 4- 5 μm as a function of the deviation angles for different magnetic field strengths. The deviation angle is the deviation from the magnetic field lines.	153
Figure 4.33. j-v plots for photocurrent density measurement of p-Cu ₂ O nanowires synthesized in various magnetic fields. The annealing temperature of Cu(OH) ₂ nanowires: 450°C.	155
Figure 4.34. j-v plots for photocurrent density measurement of sample 3 annealed at various temperatures.	156
Figure 4.35. Comparison of photocurrent density generation before and after the coating of the blocking layer (a), and Nyquist plots showing the impedance spectra of the planar Cu ₂ O and Cu ₂ O nanowires.	157
Figure 4.36. Stability analysis of p-Cu ₂ O nanowires for 75 min in 0.5 M Na ₂ SO ₄ (pH 6) (a), and collection of H ₂ via GC analysis (b).	158

Figure 4.37. SEM micrograph images of n-Cu ₂ O films deposited on FTO substrate for (a) 5 minutes, (b) 15 minutes, (c) 25 minutes, and (d) 35 minutes.	160
Figure 4.38. XRD-peaks analysis of Cu ₂ O p-n homojunction samples synthesized at various deposition times. Samples e, f, g, and h correspond to the deposition times of 5 min, 15 min, 25 min, and 35 mins respectively.....	162
Figure 4.39. Determination of the UV-visible absorption spectra of p-n homojunction samples (a), and bandgap estimation of p-n homojunction samples using the Tauc plot.....	163
Figure 4.40. Mott-Schottky plots of Cu ₂ O p-n homojunction samples coated with various film thicknesses of n-Cu ₂ O viz. (a) 32 nm, (b) 50 nm, (c) 86 nm and (d) 94 nm.....	164
Figure 4.41. Photocurrent density determination of Cu ₂ O nanowires based p-n homojunction in an electrolyte of pH 6 (a), and schematic diagram representing the working principle of a Cu ₂ O p-n homojunction (b).	164
Figure 4.42. SEM micrographic images of Cu ₂ O p-n homojunction at different magnification scales.....	165
Figure 4.43. Schematic band diagram of the constructed Cu ₂ O nanowires based p-n homojunction samples, at equilibrium and in the dark.....	165
Figure 4.44. Stability analysis of bare p-n homojunction in 0.5 M Na ₂ SO ₄ electrolyte (pH 6) under A.M. 1.5 G illumination.....	166
Figure 4.45. Stability analysis of Cu ₂ O p-n homojunction co-catalyzed with MoS ₂ HER catalyst (a), and collection of H ₂ generation via GC analysis (b).....	167
Figure 4.46. XRD peak analysis of KTaO ₃ synthesized with different concentrations of the precursor solution of KOH.	169
Figure 4.47. Photocurrent density measurements of KTaO ₃ prepared from 10, 20, and 30 M KOH solutions and annealed at 170°C.....	170
Figure 4.48. SEM micrographic images of prepared KTaO ₃ powdered sample synthesized in 20 M KOH solution at a magnification of (a) 10 kX, and (b) 25 kX	171
Figure 4.49. UV-visible absorption spectra of various thicknesses of KTaO ₃ films deposited onto the FTO substrates	171
Figure 4.50. Determination of photocurrent density generation for Cu ₂ O nanowires based p-n homojunction samples coated with different wt. % of KTaO ₃ films.....	172
Figure 4.51. Current vs. time plot for the photo-electrodeposition of MoS ₂ on the protected p-n homojunction at -0.1 v for various time periods. Electrolyte used was 2 mM ammonium tetrathiomolybdate ((NH ₄) ₂ MoS ₄ + 0.1 M N ₂ H ₂).	173

Figure 4.52. Determination of the photocurrent density of the protected Cu ₂ O p-n homojunction with and without the coating of co-catalyst MoS ₂	174
Figure 4.53. Long-term stability analysis of the KTaO ₃ protected Cu ₂ O p-n homojunction co-catalyzed with MoS ₂ (a), and collection of the amount of H ₂ through GC analysis.....	176
Figure 4.54. Photocurrent density measurements of KTaO ₃ protected Cu ₂ O p-n homojunction co-catalyzed with mos ₂ at various pH values and in the presence of ethanol sacrificial agent.....	175
Figure 4.55. Comparative analysis of impedance measurements at each stage of photocathode modification. Inset is the modified Randle's circuit.....	178
Figure 4.56. Performance evaluation of the developed cathode (a) long-term stability test in pH 4 under continuous electrolyte renewal and in the presence of 1500 mg/l of ethanol, (b) collection of the amount of H ₂ through GC analysis, and (c) determination of H ₂ generation with various weight ratios of ethanol. Note - the red marks in the long-term stability analysis plot (a) show the electrolyte refills at the following times: 5.2 h, 10.9 h, 28.3 h, 41.0 h, 53.5 h, 57.9 h, 66.4 h, 70.1 h, 78.2 h, and 84.2 h.	178
Figure 4.57. Crystallographic composition of the protected Cu ₂ O nanowires based p-n homojunction cathode co-catalyzed with MoS ₂ . K: KTaO ₃ , M: MoS ₂	180
Figure 4.58. SEM micrographic images of (a) p-Cu ₂ O nanowires, (b) p-Cu ₂ O nanowires/n-Cu ₂ O homojunction, (c) p-Cu ₂ O nanowires/n-Cu ₂ O homojunction/KTaO ₃ overlayer, and (d) p-Cu ₂ O nanowires/n-Cu ₂ O homojunction/KTaO ₃ overlayer/MoS ₂ HER catalyst. ...	181
Figure 4.59. Elemental composition analysis by EDX spectroscopy of the developed photocathode.....	182
Figure 4.60. Analysis of the UV-visible absorption spectra for various stages of cathode modification.....	182
Figure 4.61. Determination of IPCE % with respect to the wavelength for the un-modified and modified photocathodes.....	184
Figure 4.62. Determination of the crystallographic composition before and after the long-term use of photocathode.....	185
Figure 4.63. SEM micrographic images of the (a) unused photocathode, and (b) used photocathode.....	186
Figure 4.64. Analysis of the surface by the optical microscope of (a) unused photocathode, and (b) used photocathode.....	187

Figure 4.65. XRD peak analysis of synthesized BiVO_4 by solid-state reaction, using various weights of NaHCO_3	190
Figure 4.66. Determination of photocurrent density generation of synthesized pure BiVO_4 synthesized by the solid-state method with (a) various weights of NaHCO_3 , and (b) at various annealing temperatures.	189
Figure 4.67. Confirmation of elemental composition of BiVO_4 synthesized by solid-state reaction method.	190
Figure 4.68. XRD diffraction patterns of BiVO_4 synthesized by the co-precipitation method using various weights of urea.	190
Figure 4.69. Determination of photocurrent density generation of intrinsic BiVO_4 synthesized by co-precipitation method by using different amounts of urea (a), and annealed at various temperatures (b).....	193
Figure 4.70. Determination of crystallographic phases of BiVO_4 synthesized from the hydrothermal method.....	192
Figure 4.71. Photocurrent density measurement of BiVO_4 synthesized from the hydrothermal route.	192
Figure 4.72. XRD peak analysis of doped BiVO_4 samples synthesized from the solid-state reaction method.	193
Figure 4.73. Photocurrent density determination of doped BiVO_4 synthesized from the solid-state reaction method.	194
Figure 4.74. Comparative analysis of charge carrier densities of pristine and doped BiVO_4 using Mott-Schottky plots.	196
Figure 4.75. Crystallographic analysis of Mo-W doped BiVO_4 coated with Co-Pi of various film thicknesses.	198
Figure 4.76. Determination of photocurrent densities of Mo-W doped $\text{BiVO}_4/\text{Co-Pi}$ in an electrolyte of pH 4.....	199
Figure 4.77. Determination of charge transfer resistance from the Nyquist plots of Mo-W doped $\text{BiVO}_4/\text{Co-Pi}$	200
Figure 4.78. Analysis of the optical absorption spectra of Mo-W doped $\text{BiVO}_4/\text{Co-Pi}$ by UV-visible spectroscopy.....	200
Figure 4.79. Stability analysis of Mo-W doped $\text{BiVO}_4/\text{Co-Pi}$ in an electrolyte of pH 4.....	201
Figure 4.80. XRD peak analysis of Mo-W doped $\text{BiVO}_4/\text{Co-Pi}/\text{NiFeO}_x$	201

Figure 4.81. Photocurrent density measurement of Mo-W doped BiVO ₄ /Co-Pi/NiFeO _x for different deposition times of NiFeO _x (a), and for the sample with NiFeO _x coated for 15 minutes in electrolytes of various pH values (b).	202
Figure 4.82. Impedance studies of Mo-W doped BiVO ₄ /Co-Pi/NiFeO _x for various deposition times of NiFeO _x (a), and in electrolytes of various pH values (b).	204
Figure 4.83. FESEM images of the pristine BiVO ₄ (a) and Mo-W doped BiVO ₄ /Co-Pi/NiFeO _x (b) at the magnification of 50 kX. The inset image shows the enlarged views at the magnification of 80 kX.....	207
Figure 4.84. Analysis of the optical spectra of BiVO ₄ at each modification step (a), and determination of the bandgap values of BiVO ₄ at each modification step (b).	206
Figure 4.85. Digital images of (a) pristine BiVO ₄ , and (b) Mo-W doped BiVO ₄	207
Figure 4.86. Determination of photocurrent density of BiVO ₄ at each modification step in an electrolyte of pH 9.	207
Figure 4.87. Comparative analysis of the R _{ct} values of BiVO ₄ at each modification step using the Nyquist plots.....	208
Figure 4.88. Mott-Schottky analysis of BiVO ₄ at various modification steps.	209
Figure 4.89. Stability analysis of Mo-W doped BiVO ₄ /Co-Pi/NiFeO _x in an electrolyte of pH 9 (a), and pH 4 (b).	211
Figure 4.90. The response of abpe with respect to the applied potentials for Mo-W doped BiVO ₄ /Co-Pi/NiFeO _x	211
Figure 4.91. IPCE measurement of Mo-W doped BiVO ₄ /Co-Pi/NiFeO _x in an electrolyte of pH 9.	212
Figure 4.92. Analysis of the surface morphology of (a) working electrode, and (b) counter electrode.....	214
Figure 4.93. CV plots for confirmation of adhesiveness of deposited films of (a) TiO ₂ photocatalyst for the WE, and (b) Pt photocatalyst for the CE.	215
Figure 4.94. Impedance studies of (a) WE, (b) CE of the prepared DSSC, and the Randle's circuit used to model the experimental data (c).....	216
Figure 4.95. j-V plot for the prepared DSSC under dark and illumination conditions.....	217
Figure 4.96. j-v plots of two DSSCs in series combination under dark and illumination conditions.....	219
Figure 4.97. LSV measurements for the coupled PEC device in an electrolyte of pH 4. Ethanol (1500 mg/L) was used as a sacrificial agent.	221

Figure 4.98. Stability analysis of the PEC device coupled to the two DSSCs in series combination in an electrolyte of pH 4.....	226
Figure 4.99. Collection of H ₂ generation by the unassisted stand-alone PEC device driven by two DSSCs in series	227

LIST OF TABLES

Table 2.1. Summary of some of the well-studied photoelectrode materials for PEC water-splitting.....	31
Table 2.2. Examples of photoactive oxynitride materials and their structural and electronic properties.....	37
Table 2.3. List of some of the promising p-n junctions based PEC devices.....	40
Table 2.4. List of some of the widely studied carbon-based photoelectrodes used for PEC water-splitting.....	41
Table 2.5. List of some of the dye-sensitized photoelectrodes based PEC devices.....	43
Table 2.6. List of performances of PEC reactors based on dual-photoelectrodes.....	47
Table 2.7. Summary of some of the widely studied PEC/PV (conventional solar-cells) based water-splitting.....	50
Table 2.8. Some of the well-studied multijunction PEC/PV configurations and their performances towards solar water-splitting.....	52
Table 2.9. List of a few PEC/DSSC configurations and their efficiencies for solar water-splitting.....	53
Table 2.10. Some of the noteworthy theoretical studies carried out on surface engineering and material design for effective pec water-splitting.....	55
Table 3.1. List of bath pH values for the deposition of Cu ₂ O and the corresponding observations.....	70
Table 3.2. List of deposition potentials for Cu ₂ O and the corresponding observations.....	70
Table 3.3. List of deposition periods and the corresponding observations.....	71
Table 3.4. List of photocurrent density values of p-Cu ₂ O nanowires samples prepared under various magnetic field strengths and annealed at 450°C.....	75

Table 3.5. The deposition conditions and the corresponding observations of n-Cu ₂ O coatings over the p-Cu ₂ O nanowires.....	81
Table 3.6. List of samples of KTaO ₃ prepared under different synthesis conditions.	83
Table 3.7. List of the values of weight % of MoS ₂ deposited over the protected Cu ₂ O photocathode over various deposition time periods.	85
Table 4.1. Cu ₂ O film thickness determination by the optical profilometer and from the current-time plots using the Faraday's laws of electrolysis.	105
Table 4.2. Determination of the crystal grain size, dislocation density, and the lattice strain of Cu ₂ O thin films deposited at various electrolyte ph.	108
Table 4.3. Determination of the bandgap and positions of the band-edges at various bath pH values of Cu ₂ O.....	116
Table 4.4. Effect of the bath pH on the electro/photoelectrochemical properties of Cu ₂ O thin films.....	119
Table 4.5. Comparison of the measured and the calculated film thicknesses of Cu ₂ O films electrodeposited at various deposition potentials.	129
Table 4.6. List of the values of FWHM and crystal grain sizes of Cu ₂ O electrodeposited at various potentials.....	130
Table 4.7. List of the values of charge carrier densities of Cu ₂ O deposited at various deposition potentials.....	134
Table 4.8. Determination of the influence of deposition time on the film thicknesses.	137
Table 4.9. List of the values of crystal grain size, dislocation densities, and lattice strains as a function of deposition time.....	139
Table 4.10. List of Cu ₂ O film bandgaps with respect to the deposition times.	143
Table 4.11. List of flatband potentials and charge carrier densities as a function of deposition times.....	145
Table 4.12. The FWHM values along with the standard deviations obtained from the Gaussian fitting of the angular distribution curves of nanowires corresponding to different magnetic field strengths. The table also summarizes the nanowire mean diameters as measured by the ImageJ software, and the demagnetization factor values for each magnetic field strength.	154
Table 4.13. Values of photocurrent densities with respect to the aspect ratio of nanowires synthesized at various magnetic field strengths.	155

Table 4.14. Performance of sample c after being annealed at various temperatures in an inert atmosphere of N ₂	156
Table 4.15. Determination of film thickness of n-Cu ₂ O over the surface of p-Cu ₂ O nanowires deposited for various time periods.....	160
Table 4.16. Values of crystal sizes of n-Cu ₂ O over the surface of p-Cu ₂ O nanowires with respect to the photo-electrodeposition time periods.	161
Table 4.17. List of the values of bandgaps of KTaO ₃ synthesized with 20 M KOH, as a function of film thicknesses of KTaO ₃	171
Table 4.18. List of the values of weight % of MoS ₂ deposited onto the protected cathode as a function of various photo-deposition time periods.....	173
Table 4.19. Values of photocurrent densities of developed cathode at various pH values....	176
Table 4.20. List of the photoelectrochemical parameters of Mo-W doped BiVO ₄ /Co-Pi/NiFeO _x in various electrolyte pH values.....	202
Table 4.21. List of the charge transfer values of Mo-W doped BiVO ₄ /Co-Pi/NiFeO _x at various pH values.	204
Table 4.22. List of optical and photoelectrochemical properties of BiVO ₄ at each modification step.....	207
Table 4.23. List of the electrochemical properties of BiVO ₄ at each modification step.	209
Table 4.24. List of photovoltaic parameters of the in-house built DSSC.....	217
Table 4.25. List of the photovoltaic properties of the in-house built DSSC and two DSSCs in series combination.	219

LIST OF ABBREVIATIONS

ABPE	Applied bias-to-photon efficiency
A.M.	Air Mass
CB	Conduction band
CE	Counter electrode
CPE	Constant phase element
CV	Cyclic voltammetry
DSSC	Dye-sensitized solar cell

EIS	Electrochemical impedance spectroscopy
FF	Fill factor
FTO	Fluorine-doped tin oxide coated glass
HEC	Hydrogen-evolution catalyst
HER	Hydrogen-evolution reaction
HOMO	Highest occupied molecular orbital
IPCE	Incident photon-to-current conversion efficiency
LSV	Linear sweep voltammetry
LUMO	Lowest unoccupied molecular orbital
NHE	Normal hydrogen electrode
OCP	Open-circuit potential
OER	Oxygen evolution reaction
PEC	Photoelectrochemical
PV	Photovoltaic
RE	Reference electrode
RHE	Reversible hydrogen electrode
STH	Solar-to-hydrogen
UV	Ultraviolet
VB	Valence band
WE	Working electrode
WOC	Water-oxidation catalyst

LIST OF ACRONYMS

A	Optical absorbance
---	--------------------

α	Absorptivity
β_{hkl}	Full width half maximum (FWHM)
C_{sc}	Space-charge capacitance
d	Mean diameter of nanowires
E_F	Fermi-level energy
E_g	Bandgap energy
ΔE°	Standard cell potential
e^-	Electrons
ϵ	Relative permittivity
ϵ_0	Permittivity of free space
h^+	Holes
$h\nu$	Energy of incident light
I_a	Anodic peak of CV plot
I_c	Cathodic peak of CV plot
j_p	Photocurrent density
j_{sc}	Short-circuit current
l	Mean length of nanowires
m^*	Effective mass of holes
N_A	Acceptor density
N_D	Dopant density
N_V	Effective density of states in the valence band
N_d	De-magnetization factor
η_F	Faradaic efficiency
P	Rate of power of incident light
P_{mono}	Rate of power of monochromatic incident light

Q	Constant phase element
R_{ct}	Charge transfer resistance
R_s	Solution or series resistance
V_{app}	Applied potential
V_{fb}, V_f	Flatband potential
V_{bi}	Built-in potential
$V_{Ag/AgCl}$	Potential at Ag/AgCl scale
$V^0_{Ag/AgCl}$	Standard potential of Ag/AgCl
V_{RHE}	Potential at RHE scale
W	Warburg's impedance
Z	Impedance
Z'	Real part of the impedance
Z''	Imaginary part of the impedance